Transport Time Scales in Soil Erosion Modelling

I. G. Lisle [1], G. C. Sander [2*], J.-Y. Parlange [3], C.W. Rose [4], W. L. Hogarth [5], R. D. Braddock [4], F. Stagnitti [6], D. A. Lockington [7], S. Jomaa [8], M. Cheraghi [9], D. A. Barry [9]

[1] Deceased

[2] School of Civil and Building Engineering, Loughborough University, Loughborough, LE11 3TU United Kingdom. Ph. +44 (1509) 223-777. g.sander@lboro.ac.uk

[3] Department of Biological and Environmental Engineering, Cornell University, Ithaca, New York 14853-5701 USA. Ph. +1 (607) 255-2476. jp58@cornell.edu

[4] Environment, Planning and Architecture, Griffith University, Nathan, Queensland 4111 Australia. Ph. +61 (7) 3735-7397, +61 (7) 3735-7516. c.rose@griffith.edu.au, r.braddock@griffith.edu.au

[5] Faculty of Science and Information Technology, University of Newcastle, University Drive, Callaghan, NSW 2308 Australia. Ph. +61 (7) 3875-7431. bill.hogarth@newcastle.edu.au

[6] Federation University Australia, Ballarat, Victoria 3353 Australia. Ph. +61 (3) 5327-9745. f.stagnitti@federation.edu.au

[7] School of Civil Engineering, The University of Queensland, St Lucia, 4072 Australia. Ph. +61 (7) 3365-4054. d.lockington@uq.edu.au

[8] Department of Aquatic Ecosystem Analysis and Management (ASAM), Helmholtz Centre for Environmental Research – UFZ, Brückstr. 3a, 39114 Magdeburg, Germany. Ph. +49 (391) 810-9135. seifeddine.jomaa@ufz.de

[9] Laboratoire de technologie écologique (ECOL), Institut d'ingénierie de l'environnement (IIE), Faculté de l'environnement naturel, architectural et construit (ENAC), Station 2, Ecole Polytechnique Fédérale de Lausanne (EPFL), 1015 Lausanne, Switzerland. Ph. +41 (21) 693-5576, +41 (21) 693-5919. mohsen.cheraghi@epfl.ch, andrew.barry@epfl.ch

Submitted to: *Vadose Zone Journal*, 9 June 2017

Accepted 16 September 2017

[*] To whom correspondence should be addressed

Core Ideas

- Erosion time scales inherent in the Hairsine-Rose soil erosion are exposed
- Both fast and slow time scales are isolated, and can be estimated a priori
- The maximum sediment settling rate controls the possible range of timescales
- In practice, the full range of erosion time scales are not seen in flume experiments

Abstract

Unlike sediment transport in rivers, erosion of agricultural soil must overcome its cohesive strength to move soil particles into suspension. Soil particle size variability also leads to fall velocities covering many orders of magnitude, and hence to different suspended travel distances in overland flow. Consequently, there is a large range of inherent time scales involved in transport of eroded soil. For conditions where there is a constant rainfall rate and detachment is the dominant erosion mechanism, we use the Hairsine-Rose (HR) model to analyze these timescales, to determine their magnitude (bounds) and to provide simple approximations for them. We show that each particle size produces both fast and slow timescales. The fast timescale controls the rapid adjustment away from experimental initial conditions – this happens so quickly that it cannot be measured in practice. The slow time scales control the subsequent transition to steady state and are so large that true steady state is rarely achieved in laboratory experiments. Both the fastest and slowest time scales are governed by the largest particle size class. Physically, these correspond to the rate of vertical movement between suspension and the soil bed, and the time to achieve steady state, respectively. For typical distributions of size classes, we also find that there is often a single dominant time scale that governs the growth in the total mass of sediment in the non-cohesive deposited layer. This finding allows a considerable simplification of the HR model leading to analytical expressions for the evolution of suspended and deposited layer concentrations.

Keywords: Erosion, transport, timescales, multi-size, detachment

1. Introduction

Human-induced soil erosion is a worldwide problem with significant economic and environmental costs. Loss of surface soil leads to a reduction in soil fertility, structure and resilience, an ultimately leads to non-productive land and desertification (Lal, 2001). Sediment is a pollutant in its own right. It reduces light penetration and damages freshwater ecosystems. In addition, it is a carrier of pollutants such as pesticides, phosphorus and bacteria, which promote eutrophication and microbial contamination of surface water bodies. The growth of hypoxic zones in coastal waters is related directly to river discharges containing high levels of sediment-sorbed nutrients originating from agricultural runoff. Such zones occur in the Baltic, Black and East China Seas, and in the Gulf of Mexico (Boesch et al., 2009; Diaz and Rosenberg, 2008). As contaminants bind preferentially to clay and silt particles, predicting their transported loads also requires the ability to predict the particle size distribution of the eroded sediment.

Depending on the spatial scale of sediment transport, there is a range of timescales involved that determine transport behavior at that spatial scale. There is an associated advective timescale for transport in suspension, a morphological timescale associated with bedform evolution (Fowler, 2011; McGuire et al., 2013), and a timescale for sediment to move through and exit a catchment. These different timescales depend on the soil's particle size or settling velocity distribution since this influences how sediment moves down a laboratory flume or through a landscape. In addition, the size distribution of deposited sediment at the beginning of an erosion event affects transported sediment fluxes for the different particle sizes (Cheraghi et al., 2016; Kim et al., 2013; Sander et al., 2011). From simulations using the Hairsine-Rose (HR) model (Hairsine and Rose, 1991, 1992b), Sander et al. (2011) confirmed that the particle size distribution and the initial surface conditions of a soil determine not only the formation but also the shape of hysteretic loops for suspended sediment concentration-versus-volumetric flow rate, as seen in experimental data (Eder et al., 2010; Oeurng et al., 2010; Seeger et al., 2004; Williams, 1989). Clockwise, anti-clockwise and figure eight (both flow orientations) hysteresis loops are straightforward to obtain using the HR model. Physical explanations of the formation of the different hysteresis loops are based on the availability of easily erodible sources of sediment and its spatial distribution at the start of an erosion event (Oeurng et al., 2010; Smith and Dragovich, 2009). These sediment sources correspond to the readily erodible finer sediments as well as material in the low-cohesion deposited layer of the HR model. The model's prediction of different hysteretic curves arises from its specification of the initial size class distribution of this layer along with its evolution, and that of the suspended sediment.

Recently, Cheraghi et al. (2016) tested the performance of the HR model against a series of hysteretic experiments and found that it captured the behavior of all particle sizes. While hysteresis was clearly shown to occur for the smaller particles, there was very little, if any, hysteresis behavior for the larger particles. Sander et al. (2011) and Cheraghi et al. (2016) demonstrated that a significant factor determining the size, shape and orientation of hysteresis loops is the difference between the supply limit of fine sediment and transport limit of coarse sediment, along with spatial variability in the state of the initial soil surface. This distinction is an important attribute of any erosion model (Kirby, 2010). Kim et al. (2013) used a two-dimensional numerical solution of the HR model and St Venant equations to analyses sediment transport through the Lucky Hills watershed in Walnut Gulch. They also showed the importance of watershed geometry and morphological evolution on the supply and transport-limited movement of sediment sizes throughout the watershed.

With the growth of computational power along with the development of accurate, reliable and efficient numerical schemes, landscape and catchment scale soil erosion modelling using the HR formulation is possible (Fiener et al., 2008, Van Oost et al., 2004). For example, Le et al. (2015) developed a two-dimensional scheme for which the stability criteria for time stepping is solely governed by the Courant-Friedrichs-Lewy condition for the St Venant equations. This is a significant advance over the schemes of Heng et al. (2009, 2011) and Kim et al. (2013), where the controlling stability criterion was determined by the fall velocity of the largest size class. Kim and Ivanov (2014) used a combined multi-dimensional HR, St Venant and morphological model to study catchment-scale movement of eroded sediment, the scale dependence of erosion rates and the associated contaminant and nutrient fluxes.

Kim and Ivanov (2014) noted that a controlling factor determining non-uniqueness of sediment yield is the two timescales controlling the rapid rise to the peak concentration and the slow decay to steady state. These two timescales were previously noted and discussed by Sander et al. (1996) and Parlange et al. (1999), who developed an approximate analytical expression for the HR model. The solution of Parlange et al. (1999) shows the importance of the largest size class in determining the time for steady state to be achieved. However, there remains the question of how the underlying soil properties determine these two transport time scales. Kim and Ivanov (2014) showed there is a relationship with the dimensionless Shields parameter. However, the more fundamental connection with soil properties, sediment size distribution, rainfall rate, and erodibility of both the original and deposited soil was not considered.

Below, we show that due to the distribution of sediment sizes in a given soil, there is a wide range of associated time scales that occur under rainfall detachment-controlled soil erosion. Not only do we determine precise expressions for these, we show how these timescales combine to control the overall behavior of the rapid rise in suspended sediment concentration and the slow decline to steady state. In addition, we examine these time scales in terms of (i) what can be realistically measured in the laboratory, and (ii) how they result in a rapid movement to a quasi-equilibrium state between the deposited layer and the suspended sediment. In order to make our analysis more tractable, a number of simplifying assumptions are invoked. These are that (i) there is a constant rainfall rate, (ii) rainfall detachment is the dominant erosion mechanism and that shear-driven entrainment processes can be neglected, (iii) only net erosion conditions occur and (iv) the breakdown of aggregates (which change the soil's settling velocity distribution) is not considered.

We note that this is the first time where such an analysis has been performed that relates erosion timescales to both soil and hydraulic properties, for a multi-size class soil. There is a need to understand the intrinsic behaviour of the models that are built, rather than just curve fitting or calibrating them to data as a means of demonstrating their validity. Many complex models have been developed without investigating their mathematical properties, other than a sensitivity analysis to parameters. This does not inform users as to whether the functional dependence of the model output to these parameters is physically sensible, except for the very small sensitivity range that was tested. In our analysis, we are able to determine simple formulas that elucidate the effect on the solution behaviour of the HR model for all physically relevant values of the soil and hydraulic parameters. Consequently we can explain and interpret what these formulas imply both physically and mathematically, and therefore gain further scientific understanding of erosion modelling.

2. HR model and solutions

Under the just-given assumptions, the one-dimensional HR model for mass conservation of water and eroded sediment is given by the following system of equations (Hairsine and Rose, 1991, 1992b),

$$\frac{\partial (Dc_i)}{\partial t} + \frac{\partial (qc_i)}{\partial x} = e_i + e_{di} - d_i, \quad i = 1, \ldots, I, \tag{1}$$

$$\frac{\partial m_i}{\partial t} = d_i - e_{di}, \quad i = 1, \ldots, I, \tag{2}$$

$$\frac{\partial D}{\partial t} + \frac{\partial q}{\partial x} = R, \tag{3}$$

where t is time (s), x is downstream distance (m), D is flow depth (m), q is the water flux per cross-sectional width (m^2 s^{-1}), c_i is the suspended sediment concentration in size class i (kg m^{-3}), m_i is the mass per unit area of deposited sediment of size class i (kg m^{-2}), and I is the total number of sediment size classes. Eq. (3) is the kinematic approximation to the Saint-Venant equations (Wooding, 1965). The excess rainfall rate, R (m s^{-1}), is the difference between the rainfall rate, P, and the infiltration rate through the soil.

The conceptual layout of the HR model is shown in Fig. 1. The source terms on the right side of Eqs. (1) and (2) represent the processes of raindrop detachment of original uneroded cohesive soil, e_i, and the non-cohesive deposited layer, e_{di}, respectively (kg m^{-2} s^{-1}), and deposition of suspended sediment due to gravity, d_i (kg m^{-2} s^{-1}). Note that Eq. (2) states that there is no flux component moving sediment within the deposited layer, and that changes in its mass are due to differences in erosion and deposition rates.

Expressions for the rainfall detachment and deposition rates are (Hairsine and Rose, 1991, 1992b):

$$e_i = ap_i P(1-H), \qquad e_{di} = a_\mathrm{d} PH\frac{m_i}{m}, \qquad d_i = \vartheta_i c_i, \tag{4}$$

and following Sander et al. (1996), the HR model can be written as:

$$D\frac{\partial c_i}{\partial t} + q\frac{\partial c_i}{\partial x} = ap_i P(1-H) + a_\mathrm{d} PH\frac{m_i}{m} - \vartheta_i c_i - Rc_i, \quad i = 1, \ldots, I, \tag{5}$$

$$\frac{\partial m_i}{\partial t} = \vartheta_i c_i - a_\mathrm{d} PH\frac{m_i}{m}, \quad i = 1, \ldots, I. \tag{6}$$

The remaining parameters in Eq. (5) are the detachability, a (kg m^{-3}), of the original soil, the redetachability, a_d (kg m^{-3}), of the deposited soil, settling velocities, ϑ_i (m s^{-1}), and proportion of mass in each size class, p_i (with $\Sigma p_i = 1$). The total mass of soil in the deposited layer is $m = \sum_{i=1}^{I} m_i$, with H ($0 \le H \le 1$) determining the level of protection provided by the deposited layer to the original underlying soil:

$$H = \min\left(1, \frac{m}{m^*}\right). \tag{7}$$

The parameter m^* (kg m^{-2}) is the total mass required for complete protection by the deposited layer (i.e., $H = 1$).

Physically, Eq. (4) means that the detachment or redetachment rates, respectively, of a particle size are proportional to the rainfall rate, availability through p_i or m_i/m, and accessibility of the particles through $1 - H$ or H, respectively. The detachability, a, and redetachability, a_d, are decreasing functions of both the soil's cohesive strength and the overland flow depth, and since the deposited layer is non-cohesive, $a_\mathrm{d} \gg a$.

The underlying time scales are found with the simplifications of the HR model used by Sander et al. (1996). These are (i) that temporal changes in c_i and m_i dominate over spatial gradients and (ii) that q and D can both be replaced by average (constant) values. This approximation was used to analyze effluent flume data under a variety of experimental conditions (Hogarth et al., 2004b; Jomaa et al., 2010, 2012; Sander et al., 1996). Laboratory erosion experiments are typically conducted in flumes using an impervious base with a saturated soil and/or with high precipitation rates. In either case, infiltration can be neglected and $R = P$. Since D, a and a_{d} are constants, we define the following dimensionless variables and parameters:

$$\tau = \frac{Pt}{D}, \quad C_i = \frac{Dc_i}{m^*}, \quad M_i = \frac{m_i}{m^*}, \quad \nu_i = \frac{\vartheta_i}{P}, \quad \alpha = \frac{a_{\mathrm{d}} D}{m^*}, \quad \beta = \frac{aD}{m^*}. \tag{8}$$

Eqs. (5)-(7) then reduce to the following linear system of 2I ordinary differential equations:

$$\frac{dC_i}{d\tau} = \beta\left(1-H\right) p_i + \alpha M_i - (1+\nu_i)C_i, \quad i = 1,...,I, \tag{9}$$

$$\frac{dM_i}{d\tau} = \nu_i C_i - \alpha M_i, \quad i = 1,...,I, \tag{10}$$

since under net erosion conditions $m < m^*$ and Eq. (7) then becomes $H = m/m^*$. In Eqs. (9) and (10), β and α are non-dimensional detachability and redetachability coefficients, respectively, with $\alpha > \beta > 0$, and $M = \Sigma M_i = H$.

Each size class has a characteristic non-dimensional settling velocity, ν_i. We consider the case of an initially uneroded soil, and solve Eqs. (9) and (10) subject to zero initial concentrations of all size classes in the water and deposited layer, i.e., $C_i(0) = M_i(0) = 0$. Note that this problem was solved by Sander et al. (1996) in terms of the system's eigenvalues. Rather than using the method outlined in their paper, the problem is solved here using Laplace transforms as it leads to (i) approximate expressions for the eigenvalues (timescales), and (ii) additional physical insight to the underlying erosion processes. The connection between the two solution methods will then be briefly discussed.

For notational convenience, we introduce $h(\tau) = 1 - H(\tau)$. When $H(\tau) = 1$, the original soil is completely shielded from erosion by the deposited soil and when $H(\tau) = 0$, the original soil is completely exposed. In Laplace space (denoted by overbars with Laplace variable s), the solution to Eqs. (9) and (10) is:

$$\bar{C}_i(s) = \frac{s+\alpha}{\nu_i} \beta p_i \bar{K}_i(s) \bar{h}(s), \qquad \textbf{(11)}$$

$$\bar{M}_i(s) = \beta p_i \bar{K}_i(s) \bar{h}(s), \qquad (12)$$

where

$$\bar{h}(s) = \frac{1}{s} - \bar{H}(s) = \frac{1}{s} - \sum_{i=1}^{I} \bar{M}_i(s) \qquad (13)$$

and

$$\bar{K}_i(s) = \frac{\nu_i}{(s+1)(s+\alpha) + \nu_i s}. \qquad (14)$$

While solutions to Eqs. (9) and (10) can be expressed as convolution integrals, for the present we consider aspects of the Laplace domain solution, which depend on inverting $\bar{K}_i$ and $\bar{h}$. Note that the central role played by h (or H) in the solutions to Eqs. (9) and (10) is evident in Eqs. (11) and (12).

The inversion of $\bar{K}_i$ is straightforward. For $\bar{h}$, we sum Eq. (12) over i, and use the definition of $h(\tau)$ to obtain:

$$\bar{h}(s) = \frac{s^{-1}}{1+\beta\bar{K}(s)}, \tag{15}$$

where

$$\bar{K}(s) = \sum_{i=1}^{I} p_i \bar{K}_i(s) = \sum_{i=1}^{I} \frac{\nu_i p_i}{(s+1)(s+\alpha)+\nu_i s}. \tag{16}$$

From Eq. (15), the steady-state value of h, denoted h_∞, is obtained by inverting the leading order term for $s \to 0$ as (Parlange et al., 1999):

$$h_\infty = h(\tau \to \infty) = \left(1 + \frac{\beta}{\alpha}\sum_{i=1}^{I} p_i \nu_i\right)^{-1} = \frac{\alpha}{\alpha + \beta \nu_{av}}, \tag{17}$$

where $\nu_{av} = \sum_{i=1}^{I} p_i \nu_i$ is the average settling velocity.

The inversion of Eqs. (11) and (12) to recover C_i and M_i depends on the singularities of $\bar{h}(s)$ in Eq. (15). There is a simple pole at $s = 0$, the residue of which gives the steady-state value of $h(\tau)$, i.e., Eq. (17). Otherwise, residues for s satisfying

$$\beta\bar{K}(s) = -1, \tag{18}$$

are needed. Since each $\bar{K}_i$ in Eq. (16) has at most two distinct singularities, $\beta\bar{K}(s) = -1$ has at most $2I$ roots. We show in the Supplementary Material that there are indeed exactly $2I$ roots, which are all real and negative.

Equation (15) can be expressed as a rational function $\bar{h}(s) = \bar{p}(s)/\bar{q}(s)$, where $\bar{p}(s)$ is a polynomial in s and:

$$\bar{q}(s) = s\prod_{j=1}^{2I}(s-\lambda_j). \tag{19}$$

In this equation, the λ_js are the roots of $\beta\overline{K}(s) = -1$, which in general must be found numerically. Then, $\overline{h}(s)$ is expressed as:

$$\overline{h}(s) = \frac{A_0}{s} + \sum_{j=1}^{2I} \frac{A_j}{s-\lambda_j}, \tag{20}$$

where, from the steady solution to Eq. (15), $A_0 = \alpha\left(\alpha + \beta v_{av}\right)^{-1}$, and values for the other A_js can be derived from the Heaviside expansion formula. The inversion of Eq. (20) is then:

$$h(\tau) = \frac{\alpha}{\alpha + \beta v_{av}} + \sum_{j=1}^{2I} A_j \exp\left(\lambda_j \tau\right). \tag{21}$$

We see in Eq. (21) that the λ_js define the different time scales affecting the behavior of $h(\tau)$, as well as $\overline{C}_i(s)$ and $\overline{M}_i(s)$, from Eqs. (11) and (12), respectively.

2.1 Solution as Convolutions

Since $h(\tau)$ is known explicitly from Eq. (21) – albeit in general it involves finding the roots of Eq. (18) numerically – the inversion of Eqs. (11) and (12) can be expressed as convolutions. Size class masses in the deposited layer are given by:

$$M_i(\tau) = p_i \beta \int_0^{\tau} K_i(\tau - y)\, h(y) dy, \tag{22}$$

where $K_i(\tau)$ is obtained by inverting $\overline{K}_i(s)$ from Eq. (14):

$$K_i(\tau) = \frac{v_i}{r_i - R_i}\left[\exp\left(r_i \tau\right) - \exp\left(R_i \tau\right)\right]. \tag{23}$$

With Eq. (23), inversion of Eq. (11) yields:

$$C_i(\tau) = p_i \beta \int_0^{\tau} L_i(\tau - y)\, h(y) dy, \tag{24}$$

where

$$L_i(\tau) = \frac{1}{r_i - R_i}\left[\left(r_i + \alpha\right)\exp\left(r_i\tau\right) - \left(R_i + \alpha\right)\exp\left(R_i\tau\right)\right]. \tag{25}$$

By summing Eq. (22), H takes the form of an integral equation:

$$H\left(\tau\right) = 1 - h\left(\tau\right) = \beta\int_0^\tau K\left(\tau - y\right)h(y)\,dy, \tag{26}$$

where $K = \sum_{i=1}^{I} p_i K_i$.

The constants R_i and r_i in Eqs. (23) and (25) are the roots of the quadratic in the denominator of Eq. (14), i.e., for each particle size class, i,

$$\begin{bmatrix} r_i \\ R_i \end{bmatrix} = -\frac{\nu_i + \alpha + 1}{2}\left[1 \mp \sqrt{1 - \frac{4\alpha}{\left(\nu_i + \alpha + 1\right)^2}}\right]. \tag{27}$$

Since $\alpha > 0$ and $\nu_i > 0$, r_i and R_i are always real and negative. Eq. (27) also allows $\bar{K}_i(s)$ from Eq. (14) to be written as:

$$\bar{K}_i(s) = \frac{\nu_i}{r_i - R_i}\left(\frac{1}{s - r_i} - \frac{1}{s - R_i}\right). \tag{28}$$

2.2 Connection with the Solution of Sander et al. (1996)

It is useful to show the connection with the solution of Sander et al. (1996). To relate the two approaches, we briefly reproduce their result more directly. The general solution of Eqs. (9) and (10) is given by the steady-state component (superscript "steady"):

$$C_i^{steady} = \frac{\alpha\,\beta\,p_i}{\alpha + \beta\nu_{av}}, \quad M_i^{steady} = \frac{\beta\nu_i p_i}{\alpha + \beta\nu_{av}}, \quad H^{steady} = \frac{\beta\nu_{av}}{\alpha + \beta\nu_{av}}, \tag{29}$$

plus the general solution of the homogeneous equation. Substituting $C_i(\tau) = C_i^{steady} + \gamma_i \exp(\lambda\tau)$ and $M_{di}(\tau) = M_i^{steady} + \mu_i \exp(\lambda\tau)$ into Eqs. (9) and (10) and assuming 2*I* distinct eigenvalues λ_j yields:

$$C_i(\tau) = \frac{\alpha\beta p_i}{\alpha + \beta\overline{v}} + \sum_{j=1}^{2I} A_j \gamma_{ij} \exp(\lambda_j \tau), \ \ i = 1, ..., I, \tag{30}$$

$$M_i(\tau) = \frac{\beta v_i p_i}{\alpha + \beta\overline{v}} + \sum_{j=1}^{2I} A_j \mu_{ij} \exp(\lambda_j \tau), \ \ i = 1, ..., I, \tag{31}$$

where γ_{ij} and μ_{ij} are the i^{th} component of the eigenvectors associated with the j^{th} eigenvalue λ_j, and are given by:

$$\gamma_{ij} = \frac{-\beta(\lambda_j + \alpha) p_i}{(\lambda_j + 1)(\lambda_j + \alpha) + \lambda_j v_i}, \tag{32}$$

$$\mu_{ij} = \frac{-\beta v_i p_i}{(\lambda_j + 1)(\lambda_j + \alpha) + \lambda_j v_i}. \tag{33}$$

By summing Eq. (31) over the size classes and noting that $\sum_{i=1}^{I} \mu_{ij} = -\beta\overline{K}(\lambda_j) = 1$, then:

$$H(\tau) = H^{steady} + \sum_{j=1}^{2I} A_j \exp(\lambda_j \tau), \tag{34}$$

in agreement with Eq. (21). The coefficients A_j are found by matching the initial conditions $C_i(0) = 0$, $M_i(0) = 0$, and in general must be found numerically.

The characteristic equation defining the eigenvalues in Eqs. (30) and (31) is $\beta\overline{K}(\lambda) = -1$, which, not surprisingly, also appears in the Laplace transform solution through Eq. (18). The singularities arising in the inversion of $\overline{h}$ are the eigenvalues in Eqs. (30) and (31) that control the erosion timescales inherent in the HR model. Note that carrying out the integrations in Eqs. (22) and (24) – with Eq. (21) – results in Eqs. (30) and (31), respectively. The different forms of the solution allow different insights and interpretations of the erosion processes to be obtained. The temporal time scales appearing in the solutions of the HR model, and hence the effect of the soil's particle size distribution on erosion timescales, is governed by the *distribution and size of the eigenvalues*, which in general are calculated numerically. It is clear that on physical grounds we would expect that all λ_js in Eqs. (30) and (31) are negative; otherwise the solutions would diverge at large times. Consequently, it is the magnitude of the λ_js that determine the timescale over which the separate contributions through $\exp(\lambda_j \tau) \rightarrow 0$, i.e., the system approaches steady state. In the next section, we obtain simple approximations for the eigenvalues as functions of erosion parameters and the settling velocity distribution.

3. Time scale bounds

In the Supplementary Material, several results describing the behavior of the λ_js are derived formally. These results are now used to interpret time scales in the HR model physically.

Differences between soils and experimental conditions are expressed through different values of the dimensionless parameters v_i, α, and β. While the HR model imposes the physical condition $\alpha > \beta > 0$, in the Supplementary Material it is shown that α, β greater than or less than one also plays an important role in the analysis of the eigenvalues, as might be expected from the denominators of Eqs. (32) and (33). We examine in detail the case of $\alpha > \beta > 1$ as it occurs often in practice (Sander et al., 1996), and consider the slight modifications for the other two cases, $\alpha > 1 > \beta$ and $1 > \alpha > \beta$, in the Discussion.

3.1 Example soil

To illustrate the features of the solution and how the bounds on the eigenvalues are obtained, consider a soil composed of I = 3 particle sizes with fall velocities of (0.00018, 0.0033, 0.0125) m s^{-1} subject to a constant rainfall rate of 56 mm h^{-1}. This results in dimensionless fall velocities ν_1, ν_2, ν_3 of 11.57, 212.1 and 803.6, respectively. Taking $\alpha = 25$, $\beta = 20$ and $p_i = 1/3$ results in the solution curves from (9) and (10) as shown in Fig. 2. This figure shows that the total suspended sediment concentration undergoes a rapid early rise to the peak concentration, followed by an apparent exponential decline to steady state. The smallest size class makes the greatest contribution to the peak due to its lowest settling velocity and therefore tends to remain in suspension relative to the larger sediment sizes. This initial flush of fine sediment is regularly seen in experimental data and is primarily responsible for the eutrophication and pollution of surface water bodies through the additional transport of sorbed fertilizers and pesticides. The larger size classes quickly fall out of suspension and make the greatest contribution to the growth of the deposited layer and the magnitude of H. It is the rate of growth of H that determines the time of the peak concentration and for the subsequent decline in C through the reduction in access to small particle sizes. The smallest size class contributes little to H (and so to the deposited layer). Hence, the only significant source of this size class to the suspended sediment load is from the original uneroded soil. Due to the increase of H, the detachment process (i.e., raindrop-induced erosion) is unable replace the small particles that are transported downstream and so C rapidly drops off from its peak. The form of the solution curves shown in Fig. 2 remains the same for any α or β when $\alpha > \beta$. Changes in their magnitude simply change the position, magnitude and rate of decline from the peak concentration.

Returning to $\bar{K}(s)$, the form of this function for α = 25 and β = 20 is shown in Fig. 3, where we observe that the roots R_i and r_i (labeled according to their magnitude such that $|R_i| > \alpha$ and $|r_i| < 1$) from Eq. (27) separate the eigenvalues into discrete intervals. This arises because $\bar{K}(s)$ is made up from the sum of the I separate $\bar{K}_i(s)$ functions with each one approaching + or –∞ depending whether s approaches R_i or r_i from above or below. Of the 2I (six in this example) eigenvalues, I – 1 can be found between R_1 and R_I and I – 1 can be found within r_1 and r_I. The remaining two eigenvalues are located in the region between R_1 and r_1, which can be further isolated into having one each in (R_1,–α) and (–α,–1). This distribution of the eigenvalues holds for any I when $\alpha > \beta > 1$ (Supplementary Material). Thus, increasing the number of size classes between v_1 and v_3 merely adds more intervals between both –∞ and R_3, and r_3 and 0. Note that from Eq. (27), both R_i and r_i depend only on the i^{th} settling velocity, v_i, and redetachability, α, and that for $v_i \gg \alpha$, $R_i \to -v_i$ and $r_i \to 0$.

The analysis presented in the Supplementary Material, which generalizes the results shown in Fig. 3, can be summarized by the following four properties. For a soil that is composed of any number of particle size classes I, then for $\alpha > \beta > 1$:

(i) All the eigenvalues λ are real, simple and negative;

(ii) There are I eigenvalues in the interval (–∞,–α);

(iii) There are I – 1 eigenvalues in the interval (–1,0);

(iv) There is 1 eigenvalue in the interval (–α, –1).

From (i), the solution will decay towards steady state without oscillations. Further, there are no solutions having terms of the form $\tau \exp(\lambda \tau)$. Since α > 1, the eigenvalues in (ii), (iii) and (iv) can be classified as ‘fast’, ‘slow’ and ‘intermediate’, respectively, as they represent the rate at which their individual contributions to the solution become negligible as τ increases, according to the decay rates $\exp(\lambda_j \tau)$.

3.2 Eigenvalue approximations for a Black Earth soil

Sander et al. (1996) solved the system of equations given by Eqs. (9) and (10), and successfully applied the solution to the experimental data of Proffitt et al. (1991) for two different soils, Black Earth (vertisol) and Solonchak (aridisol). The experimental conditions are consistent with the assumptions given in the Introduction. As both soils behave similarly, we will present results only for the Black Earth. The experiment using the Black Earth soil had a precipitation rate of $P = 56$ mm h^{-1} and an overland flow depth of $D = 2$ mm, which results in $\alpha \approx 100, \beta \approx 50$ along with dimensionless settling velocities for 10 size classes as given in Table 1. Note the wide range in the dimensionless settling velocities ($10^{-1} – 10^{5}$).

In Table 2, the roots satisfying $\beta \overline{K}(s) = -1$ are presented along with their bounds as described in Theorems 1 and 2 in the Supplementary Material. It is straightforward to derive estimates for the fast eigenvalues, which lie in the interval $(-\infty, -\alpha)$, as they all sit very close to the corresponding R_i (Fig. 3). Thus, in a given interval i, the dominant contribution from $-\beta \sum p_i \overline{K}_i(s) = 1$ comes from the i^{th} term due to $(s – R_i)^{-1}$ in Eq. (28), and so the summation can be simplified to a single term to give $-\beta p_i K_i(s) \approx 1$ for $i = 1,2 \ldots I$, or $-\beta p_i v_i / R_i \approx s - R_i$ from Eq. (28) since $\lambda \gg r_i$. We therefore approximate the i^{th} fast eigenvalue as:

$$s_i^f = R_i - \frac{\beta \nu_i p_i}{R_i}, \tag{35}$$

which shows the weak (second-order) dependence of s^f on β. Noting that for real soils usually $\alpha + \nu_i \gg 1$, then by combining with Eq. (27) and ignoring the second-order correction, Eq. (35) simplifies to:

$$s_i^f = -(\alpha + \nu_i). \tag{36}$$

Unlike the fast eigenvalues, the values of the slow eigenvalues in the interval $(-1, 0)$ wander between the bounds r_i, so reliable expressions corresponding to Eqs. (35) and (36) are not available. The closest estimate to each slow eigenvalue is then given by the bounds r_i, which from Eq. (27) with $\alpha + \nu_i \gg 1$ gives:

$$s_i^s \approx r_i \approx -\frac{\alpha}{\alpha + \nu_i}, \quad i = 2, 3, ..., I. \tag{37}$$

Interestingly, Parlange et al. (1999) derived an approximate analytical solution to c_i and m_i based on an approach that did not consider the underlying eigenvalues. They obtained large time exponential decay terms of the form $\exp[-\alpha\tau(\alpha + \nu_i)^{-1}]$, which correspond to the timescales in Eq. (37). This helps explain the favorable comparison of their approximation with the exact analytical solution. While in general Eq. (36) is a good estimate of the fast eigenvalues as they always sit very close to R_i, Eq. (37) is less accurate for the slow eigenvalues as they can move within the bounds r_i and r_{i+1} as the soil properties change. This is the source of the small discrepancy between the approximate and exact solutions presented by Parlange et al. (1999). For instance, for the soil and parameter values used in Table 2, the best estimate for the slow eigenvalues is mostly given by the lower bound r_{i-1} rather than r_i.

For large α with $\alpha > \beta > 1$, the interval $(-\alpha,-1)$ containing the intermediate eigenvalue is large and a tighter bound would be preferred. From Theorems 1 and 2 (Supplementary Material), for the more common case of $\alpha > \beta > 0$, this interval can be considerably reduced to (s_L, s_U), where:

$$s_L > \max\left(-\alpha, -1 - \frac{\beta \sum \frac{\nu_i p_i}{r_i - R_i}}{1 - \beta \sum \frac{\nu_i p_i}{(r_i - R_i)(-\alpha - R_i)}} \right), \tag{38}$$

and

$$s_U < \min\left(-1, r_1 - \frac{\beta \sum \frac{\nu_i p_i}{r_i - R_i}}{1 - \beta \sum \frac{\nu_i p_i}{(r_i - R_i)(-1 - R_i)}} \right). \tag{39}$$

For the Black Earth soil, the value of the intermediate eigenvalue is -38.88 (Table 2), with Eqs. (38) and (39) giving the bounds of $s_L = -43.86$ and $s_U = -38.64$. Other than for $\beta = 1$ when $s = -1$ (see Remark 6.1 in the Supplementary Material), our extensive numerical simulations show that the upper bound s_U generally provides the closest estimate to the intermediate eigenvalue, as indeed it does for the Black Earth soil.

Equations (22), (24) and (26) show that, if h is known, then concentrations in suspension and the deposited layer are known explicitly. Although exact results rely on numerical calculation of the roots of $\beta\bar{K}(s) = -1$ (needed to determine h), we can estimate h by estimating $\bar{K}(s)$ in Eq. (15). From Theorem 3 (Supplementary Material), we have $\bar{K}(s) < -B/s$, where $B = \sum \nu_i p_i / (\alpha + \nu_i)$. Substituting this estimate for $\bar{K}(s)$ into Eq. (15), inverting and forcing the approximation to reach the correct steady-state value, gives the following approximation for h or $H = 1 - h$:

$$h(\tau) \approx \left(1-h_{\infty}\right)\exp\left(-\beta B\tau\right)+h_{\infty}, \text{ or } \quad H(\tau) = H^{steady}[1-\exp\left(-\beta B\tau\right)], \quad (40)$$

where h_{∞} is given by Eq. (17) and H^{steady} by Eq. (29). Figure 4 shows that Eq. (40) is potentially a useful approximation for *h*. This approximation is additionally valuable since it leads directly to analytical approximations for the complete solution to the HR model using the results in §2.1.

We have carried out simulations across a wide range of values for α and β where $\alpha > \beta > 1$, $\alpha > 1 > \beta,\ 1 > \alpha > \beta,$ with $\alpha / \beta = 1000, 100, 10$ and 2 for the particle size distributions of the three different soils of Proffitt et al. (1991), Polyakov and Nearing (2003) and Jomaa et al. (2010). All these simulations showed Eq. (40) to be a good approximation for $h(\tau)$, which improved as α/β decreased. Inspection of the simulation results showed that, independently of α, β or soil type, there is usually one and occasionally two or three of the coefficients A_j in Eqs. (30) and (31) that are at least an order of magnitude greater than the rest, and so isolate the key timescale controlling *h*. In addition, where there are two or three, they always occur for consecutive *j*s. By comparing the corresponding λ_j values with the values of βB, it was found that βB not only tracks these eigenvalues, it represents some averaged measure of them. The approximation Eq. (40) works well because so very few of the eigenvalue timescales contribute significantly to the summation term in Eq. (34) to *H*. Consequently, they can all be approximated by a single timescale and therefore a single exponential term of the form $\exp(-\beta B\tau)$.

4. Discussion

4.1 Physical interpretation of the convolution integral solution

The convolution integrals in §2.1 draw attention to the motion of a specific parcel of soil detached from the parent medium at a time $\tau = y$. The state at time τ of a soil parcel detached at an earlier time y is specified by the response functions $K_i(\tau)$, $L_i(\tau)$, given, respectively, by Eqs. (23) and (25). These functions represent the masses of this previously detached soil in the deposited layer and in suspension, respectively. At the earlier time y, a fraction $h(y)$ of the soil was exposed and the resulting detachment rate of a given size class was therefore $p_i \beta h(y)$, as detachment is not size class selective (Hairsine and Rose, 1991). These parcels then propagate through to time τ by the response functions. Thus, $C_i(\tau)$ and $M_i(\tau)$ are the integrals of detachment over all earlier times, i.e., the convolutions of Eqs. (23) and (25). The total deposited mass, $1 - h(\tau)$, is therefore an integral over its source at earlier times y, as given by Eq. (26). That is, Eq. (26) balances the present mass of sediment in the deposited layer against the mass of detached soil particles from earlier times y.

Figure 5 shows the response curves and h for the Black Earth soil for all ten grain size classes. Both K_i and L_i display a rapid initial transient and by comparison, a slow decay, however, the magnitude of the initial effect differs greatly with particle size. For a given v_i, the fast eigenvalues, λ_j^{fast}, define the timescales of the initial transients in K_i and L_i while the slow eigenvalues, λ_j^{slow}, control the decay to steady state. We also note that the majority of the $L_i(\lambda_j^{slow})$ values are far smaller than the corresponding $K_i(\lambda_j^{slow})$ values. This indicates that while suspended sediment concentrations and h can appear to be at steady state, the sediment size class distribution within the deposited layer is *still undergoing considerable adjustment*. This behavior is evident in Figs. 2 (measured and predicted total concentrations), 5 (c_i) and 6 (m_i) of Sander et al. (1996), which show that the suspended sediment concentrations are essentially at steady state, but those in the deposited layer are not. The largest particle size is also seen to provide the timescale controlling the transition to steady state (Figs. 5 and 6 of Sander et al., 1996).

4.2 Interpretation of rate processes

We saw above that the characteristic rates for the decoupled pairs have one fast rate $R_i < -\alpha$ and one slow rate $-1 < r_i < 0$ and that the values of R_i and r_i depend only on the i^{th} settling velocities, v_i, and redetachability, α. Moreover, as v_i increases (heavier sediment), the fast rate R_i gets faster, and the slow rate r_i gets slower. However, with increasing detachability, β, the fast rates reduce slightly, and the slow rates increase slightly. This is suggested in Fig. 3 through shifting of the horizontal line $-\beta^{-1}$ upwards and noting the corresponding changes in the position of the circled points. Since the eigenvalue bounds R_i and r_i depend only on α and the corresponding v_i, the eigenvalues cannot vary strongly with β. This is more noticeable as the number of size classes increase. The bounds R_i and r_i then crowd more densely on the intervals $\left(-\infty, -\alpha\right)$ and (–1, 0), giving the fast and slow eigenvalues less freedom to wander, and packing them tighter and tighter together in these intervals.

Concerning the different rates as described by the eigenvalues of the HR model, several observations can be made. These are that

(i) Fast and slow rates are associated primarily with uncoupled processes (deposition, redetachment) as they depend primarily on α and one or two settling velocities. Detachability, β, soil composition, p_i, and other settling velocities, v_i, have only minor effects on the fast and slow eigenvalues;

(ii) When $\alpha > \beta > 1$, the only eigenvalue whose location is genuinely a result of the coupled detachment process is the ‘intermediate’ eigenvalue, which is primarily determined by the detachability, β (e.g., Fig. 3). This eigenvalue is a good estimate of the dominant timescale governing the evolution of h permitting an accurate explicit approximation for $h(\tau)$ to be obtained, Eq. (40). As mentioned above, with h known (approximately), C_i and M_i can be estimated through their convolution integrals (§2.1).

(iii) The fastest and slowest rates are largely determined by the maximum settling velocity, v_{max}, and are thus associated with movement of the heaviest sediment;

Intuitively, we might expect that the fast and slow processes are associated with fast and slow settling soil particles, but *this is not the case*. Both the fastest and slowest rates are determined primarily by the *maximum* settling velocity, v_{max}. Good approximations for the fast and slow eigenvalues are given by $\lambda_i^{fast} \approx -(\alpha + v_i)$ and $\lambda_i^{slow} \approx -\alpha(\alpha + v_i)^{-1}$, respectively, assuming $\alpha > \beta > 1$. Thus, the shortest timescale (largest λ^{fast}) process is approximated by $O(-\left(\lambda_I^{fast}\right)^{-1}) \approx O((\alpha + v_{\max})^{-1})$ and is therefore associated with settling of the heaviest particles. The longest timescale (smallest λ^{slow}) process is $O(-\left(\lambda_I^{slow}\right)^{-1}) = O(1 + v_{\max} / \alpha)$ and is associated with downslope movement of these *same* particles. Note that while the spatial sediment gradient is neglected in Eq. (9), the effect of advection is still present through the $-C_i$ term on the right side of Eq. (9). The possible range of timescales is of order v^2_{max} if $v_{max} \gg \alpha$, as is generally expected in practice. In a real soil, the fastest processes (timescale 0.01 s for Black Earth) manifest themselves as an instantaneous initial jump, and cannot be resolved experimentally. Even the ‘intermediate’ rate process (timescale 3.4 s) is too fast to be measured for the Black Earth. The slow processes (timescale 5 min or more) are the ones that are observed in a laboratory experiment. However, the slowest processes (timescale 50 h for Black Earth) are sufficiently slow so that in any reasonable length experiment or rainfall event where raindrop detachment dominates, they will not have run to completion. Thus, although values of C_i and M_i may be varying slowly as measured in an ongoing laboratory experiment, usually steady state values of C_i and M_i will not be attained.

The eigenvalue spectrum for the Black Earth soil is shown in Table 2, where it can be seen how well the intermediate eigenvalue -38.88 is separated from the rest of the spectrum. Doubling the number of size classes to I = 20 has a very small impact on this eigenvalue. Thus, it is very stable to v being discretized in various ways and is therefore a property of the soil and experimental conditions. This occurs because the range of settling velocities is fixed for any given soil and therefore, the range of time scales is also fixed. For this reason, the number of size classes selected for a given soil does not have a great effect on the overall results.

The eigenvalues cover the complete possible range of rates by distributing themselves along portions of the real axis, while their specific locations depend on how the soil is divided into size classes. For instance, the fast eigenvalues are $\lambda_i \approx -\left(v_i + \alpha\right)$, so changing the number of size classes of v would give different eigenvalues. The particular values of the fast and slow rates depend as much on the discretization of soil data, through v_I, as on soil and experiment conditions (given through P, D, m^* and a_d). However, the fast eigenvalues *collectively,* and the slow eigenvalues *collectively* are soil and experiment properties and give the possible *range of timescales*.

The differences between classes of eigenvalues are further emphasized by the behavior of the associated eigenvectors. Below, we consider the eigenvectors associated with the fast, intermediate and slow eigenvalues.

Fast By replacing λ_j in Eqs. (32) and (33) with the approximation $-(\nu_j+\alpha)$, then the components of the fast eigenvectors are approximated by:

$$\gamma_{ij} \approx \frac{\beta \nu_j p_i}{(\nu_j+\alpha)(\nu_j-\nu_i)-\nu_j} \approx -\mu_{ij}. \quad (41)$$

The suspended sediment components of γ_{ij}, are approximately the same magnitude but opposite in sign to those of the deposited sediment components, μ_{ij}. Consequently, the ‘fast’ eigenvectors represent predominantly a rapid exchange of material between suspension and the deposited layer. Note, in addition, that for $i \neq j$ all the eigenvector components are small compared to that for $i = j$, hence exchange between the suspended and deposited material of a given size class depends little on the concentrations of other size classes. This highlights the weak coupling between the size classes.

Intermediate For the intermediate eigenvalue $\lambda+\alpha>0$ and hence Eqs. (32) and (33) show that the eigenvector components are of the same sign. All size classes now participate with the heavier size classes being more active in the deposited layer since as v_i increases in Eq. (33) so does μ_{ij}. At the same time, the lighter classes are more active in the suspension since γ_{ij} increases as v_i decreases in Eq. (32).

Slow These processes are associated with *resorting* of the deposited layer. From Eq. (32), $\nu_i\gamma_{ij}$ is approximated by:

$$\nu_i \gamma_{ij} \approx \frac{-\alpha\beta\nu_i p_i}{(\lambda_j + 1)\alpha + \lambda_j \nu_i} = \alpha\mu_{ij}, \tag{42}$$

since for the slow eigenvalues, $\alpha \gg -\lambda_j$. The approximation Eq. (42), shows that the slow eigenvalues and associated eigenvectors correspond to the condition where $\nu_i \gamma_{ij} - \alpha\mu_{ij} \approx 0$, or $\nu_i C_i - \alpha M_i \approx 0$. Since $dM_i / d\tau = \nu_i C_i - \alpha M_i$ and $H = \sum M_i$, this means that the deposited layer quickly obtains a state of quasi-equilibrium where $M_i \approx \nu_i C_i / \alpha$, which is then followed by a slow resorting of the actual contributions of each size class as they approach their steady state values over a long timescale. It was the recognition of this quasi-equilibrium state that was exploited by Parlange et al. (1999) to develop simple analytical expressions for $H(\tau)$, $M_i(\tau)$ and $C_i(\tau)$ that provided a good approximation to the solution given by Eqs. (30) and (31).

Short time processes occur on the timescale for vertical motion of soil particles and are related to exchange of material between the suspension and the deposited layer. At all times, there is a strong mass exchange between the soil bed and the suspension. The *net* mass exchange may, of course, be very small; at steady state there is indeed an exact balance. Any perturbation from steady state that leads to an imbalance between deposition and redetachment rates would rapidly be corrected. In practice, this happens so quickly it appears to be instantaneous, and in practical terms the soil bed is always in a state where $\nu_i C_i \approx \alpha M_i$.

4.3 Timescale dependence on detachability parameters for cases where α or $\beta < 1$

There are two further parameter cases that need to be considered, these being $\alpha > 1 > \beta$ and $1 > \alpha > \beta$. Remember that on physical grounds $\alpha > \beta$ resulting in $I - 1$ eigenvalues $< R_1$, $I - 1$ eigenvalues $> r_1$, and two in the region (R_1, r_1). Changes in the magnitudes of α and β simply reposition the two eigenvalues in (R_1, r_1) into the following two intervals (Lemma 6, Supplementary Material):

(i) $\alpha > \beta > 1$; (R_1, $-\alpha$) and ($-\alpha$, -1);

(ii) $\alpha > 1 > \beta > 0$; (R_1, $-\alpha$) and (-1, r_1);

(iii) $1 > \alpha > \beta > 0$; (R_1, -1) and ($-\alpha$, r_1).

While all three cases have I fast ($|\lambda| > 1$) eigenvalues, for $\beta < 1$ the intermediate eigenvalue is also less than unity, giving a total of I slow ($|\lambda| < 1$) eigenvalues. The special cases of $\beta = 1$ and $\alpha = \beta$ result in $\lambda = -1$ and $\lambda = -\alpha$, respectively; however, it is only the former case that has any physical significance.

For $\beta < 1$, the bounds on the intermediate eigenvalue given in Eqs. (38) and (39) are modified to (Theorem 2, Supplementary Material):

$$s_L > \max\left(s_{\min}, s_{\max} - \frac{\beta \sum \frac{v_i p_i}{r_i - R_i}}{1 - \beta \sum \frac{v_i p_i}{(s_{\min} - R_i)(r_i - R_i)}} \right), \tag{43}$$

for the lower bound and

$$s_U < \min\left(s_{\max}, r_I - \frac{\beta \sum \frac{v_i p_i}{r_i - R_i}}{1 - \beta \sum \frac{v_i p_i}{(s_{\max} - R_i)(r_i - R_i)}} \right), \tag{44}$$

for the upper bound. In the above equations ($s_{\min}$, $s_{\max}$) is given by ($-\alpha$, -1), (-1, r_1) or ($-\alpha$, r_1) for the above-listed cases (i), (ii) and (iii), respectively.

4.4 Spatial dependence

The quantity $\alpha/(\alpha+\nu_i)$ not only controls the slow timescales and hence the time to reach steady state for $x > qt/D$, but it also determines the advective transport velocity of the different sediment size classes. We show this by first defining the additional dimensionless space variable $z = Px/q$, then along with Eqs. (8) and (10), we rewrite Eq. (5) as:

$$\frac{\partial C_i}{\partial \tau}+\frac{\partial M_i}{\partial \tau}+\frac{\partial C_i}{\partial z}=\beta\left(1-H\right)p_i-C_i, \quad i=1,...,I. \tag{45}$$

As discussed in §4.2, the deposited layer rapidly adjusts itself so that deposition and redetachment are always in balance, except for very short times. Hence, rearranging Eq. (10) to:

$$M_i=\frac{\nu_i}{\alpha}C_i-\frac{1}{\alpha}\frac{\partial M_i}{\partial \tau}, \tag{46}$$

shows that $\alpha^{-1}\partial M_i/\partial\tau$ can be interpreted as the leading order correction to this balance. Differentiating Eq. (46) with respect to τ, neglecting the second-order derivative correction, and substituting into Eq. (45) gives the following approximation to Eq. (5) (Hogarth et al., 2004a):

$$\frac{\partial C_i}{\partial \tau}+\frac{\alpha}{\alpha+\nu_i}\frac{\partial C_i}{\partial z}=\frac{\alpha}{\alpha+\nu_i}\left[\beta\left(1-H\right)p_i-C_i\right], \quad i=1,...,I. \tag{47}$$

Equation (47) shows that disturbances in the individual particle concentrations will propagate down the slope with a characteristic speed of $\alpha/(\alpha+\nu_i)$, a quantity that appeared earlier as an estimate of the slow eigenvalues as given by Eq. (37). For the small particles, $\alpha \gg \nu_i$ and so $\alpha/(\alpha+\nu_i)\approx 1$. Thus, these particles travel at close to the water velocity, q/D. However, large particles with $\nu_i \gg \alpha$ travel downstream at a dimensionless speed of α/ν_i with the longest travel time therefore given by the largest particle.

Since Eq. (5) is hyperbolic, the method of characteristics shows that for a constant initial condition, solutions for $x > qt/D$, found by solving Eqs. (9) and (10), depend only on time. However solutions in the region $x < qt/D$ can depend on both x and t. For an imposed boundary condition that will result in significant spatial effects for $x < qt/D$, then our analysis will still apply to measured effluent concentrations until $t = DL/q$, for a flume of length L. However, as zero concentration boundary and initial conditions are commonly used in flume experiments on rainfall-driven erosion (e.g., Jomaa et al., 2010; Proffitt et al., 1991), then neglecting the spatial derivative will still result in a good approximation to $C_i(\tau)$ at the end of the flume even for $t > DL/q$, provided DL/q is greater than or equal to the time of the peak total concentration in C, as determined from Eqs. (9) and (10).

5 Conclusions

The approximate solution of Sander et al. (1996) to the Hairsine-Rose model is a useful means to analyze the range of timescales (denoted by λ) inherent in rainfall detachment erosion and transport of soils. The HR model divides the soil into I different size classes. There are $2I$ timescales, two for each individual particle size. The timescales are characterized as 'fast', 'intermediate' or 'slow'. For $\beta < 1$, each of the I size classes has a fast ($|\lambda| > 1$) and a slow ($|\lambda| < 1$) timescale, while for $\alpha > \beta > 1$ this total changes slightly to $I + 1$ fast and $I - 1$ slow timescales. The fast timescales govern rapid transient adjustments from the initial conditions to a state where the mass of sediment in suspension and the deposited layer are in quasi-equilibrium. In practice, this happens so quickly (less than seconds) that they are not resolved in a flume experiment. The slow timescales that govern the subsequent slow transition to steady state are predominantly controlled by the resorting of size classes in the deposited layer. There is also an additional timescale approximated by $(\beta B)^{-1}$ that provides a good estimate for determining the rate of growth of the total mass of sediment in the deposited layer. This time scale appears in analytical approximations for the suspended and deposited layer concentrations obtained in this work.

The fastest and slowest timescales are both controlled by the largest settling velocity, v_I. As v_I increases, these two timescales become faster and slower, respectively. These are interpreted as the vertical movement (deposition) and downslope travel time of this particle size class, and provide bounds that can be used, for example, to design laboratory experiment durations appropriately.

Compared to a soil with large particles, soils made up of *smaller* size classes will therefore have smaller λ^{fast} timescales and larger λ^{slow} timescales such that steady state occurs sooner. Tight bounds on all the individual eigenvalues were obtained. These are independent of the mass proportions p_i in each size class and the detachability of the original soil β. Thus, p_i and β can affect the characteristic rates to only a very limited extent and the primary determinants of the erosion timescales are the settling velocities, v_i, and redetachability (of the deposited sediment), α.

Acknowledgement

Support for this research was provided by the Swiss National Science Foundation grant 200021_144320.

References

Boesch D. and W.R. Boynton. 2009. Nutrient enrichment drives Gulf of Mexico hypoxia. EOS Trans. AGU, 90(14), 117-119.

Cheraghi, M., S. Jomaa, G.C. Sander and D.A. Barry. 2016. Hysteretic sediment fluxes in rainfall-driven soil erosion: Particle size effects. Water Resour Res 52: 8613-8629. Doi:10.1002/2016WR019314.

Diaz, R.J. and R. Rosenberg. 2008. Spreading dead zones and consequences for marine ecosystems. Science, 321, 926 – 929.

Eder, A., P. Strauss, T. Krueger and J.N. Quinton. 2010. Comparative calculation of suspended sediment loads with respect to hysteresis effects (in the Petzenkirchen catchment, Austria). J Hydrol 389: 168-176. Doi:10.1016/j.jhydrol.2010.05.043.

Fiener, P., G. Govers and K. Van Oost. 2008. Evaluation of a dynamic multi-class sediment transport model in a catchment under soil-conservation agriculture. Earth Surf Process Landf 33: 1639-1660. Doi:10.1002/esp.1634.

Fowler A.C. 2011 Mathematical Geoscience, Interdisciplinary Applied Mathematics 36. Springer-Verlag, England.

Hairsine, P.B. and C.W. Rose. 1991. Rainfall detachment and deposition: Sediment transport in the absence of flow-driven processes. Soil Sci Soc Am J 55: 320-324. Doi:10.2136/sssaj1991.03615995005500020003x.

Hairsine, P.B. and C.W. Rose. 1992a. Modeling water erosion due to overland flow using physical principles 2. Rill flow. Water Resour Res 28: 245-250. Doi:10.1029/91WR02381.

Hairsine, P.B. and C.W. Rose. 1992b. Modeling water erosion due to overland flow using physical principles. 1. Sheet flow. Water Resour Res 28: 237-243. Doi:10.1029/91wr02380.

Heng, B.C.P., G.C. Sander and C.F. Scott. 2009. Modelling overland flow and soil erosion on nonuniform hillslopes: A finite volume scheme. Water Resour Res, 45, doi:10.1029/2008WR007502.

Heng, B.C.P., G.C. Sander, A. Armstrong, J.N. Quinton, J.H. Chandler and C.F. Scott. 2011. Modelling the dynamics of soil erosion and size-selective sediment transport over nonuniform topography in flume-scale experiments. Water Resour Res 47, W02513, doi:10.1029/2010WR009375.

Hogarth, W.L., J.-Y. Parlange, C.W. Rose, G.C. Sander, T.S. Steenhuis and D.A. Barry. 2004a. Soil erosion due to rainfall impact with inflow: An analytical solution with spatial and temporal effects. J Hydrol 295: 140-148. Doi:10.1016/j.jhydrol.2004.03.007.

Hogarth, W.L., C.W. Rose, J.-Y. Parlange, G.C. Sander and G. Carey. 2004b. Soil erosion due to rainfall impact with no inflow: A numerical solution with spatial and temporal effects of sediment settling velocity characteristics. J Hydrol 294: 229-240. Doi:10.1016/j.jhydrol.2004.02.014.

Jomaa, S., D.A. Barry, A. Brovelli, G.C. Sander, J.-Y. Parlange, B.C.P. Heng and H.J. Tromp-van Meerveld. 2010. Effect of raindrop splash and transversal width on soil erosion: Laboratory flume experiments and analysis with the Hairsine-Rose model. J Hydrol 395: 117-132. Doi:10.1016/j.jhydrol.2010.10.021.

Jomaa, S., D.A. Barry, B.C.P. Heng, A. Brovelli, G.C. Sander and J.-Y. Parlange. 2012. Influence of rock fragment coverage on soil erosion and hydrological response: Laboratory flume experiments and modeling. Water Resour Res 48: W05535. Doi:10.1029/2011wr011255.

Kim, J. and V.Y. Ivanov. 2014. On the nonuniqueness of sediment yield at the catchment scale: The effects of soil antecedent conditions and surface shield. Water Resour Res 50: 1025 – 1045. doi:10.1002/2013WR01458.

Kim, J., V.Y. Ivanov and N.D. Katopodes. 2013. Modeling erosion and sedimentation coupled with hydrological and overland flow processes at the watershed scale. Water Resour Res 49: 5134-5154. Doi:10.1002/wrcr.20373.

Kirby, M.J. 2010. Distance, time and scale in erosion processes. Earth Surf Process Landf 35: 1621 – 1623.

Lal, R. 2001. Soil degradation by erosion. Land Degrad Develop. 12: 519 – 539. doi:10.1002/ldr.472.

Le, M.-H., S. Cordier, C. Lucas and O. Cerdan. 2015. A faster numerical scheme for a coupled system modelling soil erosion and sediment transport. Water Resour Res 51: 987 – 1005. doi:10.1002/2014WR015690.

McGuire, L.A., J.D. Pelletier, J.A. Gómez and M.A. Nearing. 2013. Controls on the spacing and geometry of rill networks on hillslopes: Rain splash detachment, initial hillslope roughness, and the competition between fluvial and colluvial transport. J. Geophys. Res. F Earth Surf. 118: 241-256. Doi:10.1002/jgrf.20028.

Oeurng, C., S. Sauvage and J.M. Sánchez-Pérez. 2010. Dynamics of suspended sediment transport and yield in a large agricultural catchment, southwest France. Earth Surf Process Landf 35: 1289-1301. Doi:10.1002/esp.1971.

Parlange, J.-Y., W.L. Hogarth, C.W. Rose, G.G. Sander, P. Hairsine and I. Lisle. 1999. Addendum to unsteady soil erosion model. J Hydrol 217: 149-156. Doi:10.1016/s0022-1694(99)00012-8.

Polyakov, V.O. and M.A. Nearing. 2003. Sediment transport in rill flow under deposition and detachment conditions. Catena 51: 33-43. Doi:10.1016/S0341-8162(02)00090-5.

Proffitt, A.P.B., C.W. Rose and P.B. Hairsine. 1991. Rainfall detachment and deposition: experiments with low slopes and significant water depths. Soil Sci Soc Am J 55: 325-332. Doi:10.2136/sssaj1991.03615995005500020004x.

Sander, G.C., P.B. Hairsine, C.W. Rose, D. Cassidy, J.-Y. Parlange, W.L. Hogarth and I.G. Lisle. 1996. Unsteady soil erosion model, analytical solutions and comparison with experimental results. J Hydrol 178: 351-367. Doi:10.1016/0022-1694(95)02810-2.

Sander, G.C., T. Zheng, P. Heng, Y. Zhong and D.A. Barry, 2011. Sustainable soil and water resources: Modelling soil erosion and its impact on the environment. 19th International Congress on Modelling and Simulation - Sustaining Our Future: Understanding and Living with Uncertainty, MODSIM2011, Perth, Western Australia, Australia. 12-16 December. http://www.mssanz.org.au/modsim2011/Plenary/sander.pdf.

Seeger, M., M.P. Errea, S. Beguería, J. Arnáez, C. Martí and J.M. García-Ruiz. 2004. Catchment soil moisture and rainfall characteristics as determinant factors for discharge/suspended sediment hysteretic loops in a small headwater catchment in the Spanish pyrenees. J Hydrol 288: 299-311. Doi:10.1016/j.jhydrol.2003.10.012.

Smith, H.G. and D. Dragovich. 2009. Interpreting sediment delivery processes using suspended sediment-discharge hysteresis patterns from nested upland catchments, south-eastern Australia. Hydrol Proc 23: 2415-2426. Doi:10.1002/hyp.7357.

Van Oost, K., L. Beuselinck, P.B. Hairsine and G. Govers. 2004. Spatial evaluation of a multi-class sediment transport and deposition model. Earth Surf Process Landf 29: 1027-1044. Doi:10.1002/esp.1089.

Williams, G.P. 1989. Sediment concentration versus water discharge during single hydrologic events in rivers. J Hydrol 111: 89-106. Doi:10.1016/0022-1694(89)90254-0.

Figure captions

Figure 1. Conceptual layout for the Hairsine-Rose model (Hairsine and Rose, 1991, 1992a,b).

Figure 2. Dimensionless total and particle size class suspended sediment concentrations (top plot), dimensionless deposited size classes masses and H (bottom plot) as a function of τ from Eqs. (9) and (10). Labels 1, 2 and 3 correspond to particles sizes 1, 2 and 3, respectively.

Figure 3. Plot of $\bar{K}(s)$ and $-1/\beta$ (solid lines) showing how the solutions of $\bar{K}(s) = -1/\beta$ (circled) sit in well-defined intervals defined by R_i and r_i (dashes) for i = 1, 2, 3. These are found from Eq. (27) and correspond to roots of the quadratics in the denominator of Eq. (16).

Figure 4. Comparison of exact $H(\tau) = \Sigma M_i = 1 - h(\tau)$ from Eq. (31) (solid line) and the approximation for H from Eq. (40) (dashed-dotted line) for the Black earth soil (parameter values given in Table 2).

Figure 5. Response functions K_i, (deposition, left plot) and L_i (suspension, right plot) defined by Eqs. (23) and (25), respectively, for the Black Earth soil for α = 100, β = 50 and v_i from Table 1. Each plot also shows h (dashed line) obtained from (26), which appears in the convolution integrals of Eqs. (22) and (24). The circles (two for each curve) correspond to K_i and L_i calculated at both eigenvalues corresponding to v_i. The plots show the different possible timescales for the different sediment size classes. Size class 1 ($v_i \ll \alpha$) contains the finest particles, transitional size classes correspond to i = 2, 3 ($v_i \approx \alpha$) and heavy sediment size class to $i \geq 4$ ($v_i \gg \alpha$).

Table 1. Dimensionless Black Earth particle size distribution (I = 10 size classes) for a rainfall rate of P = 56 mm h^{-1}, p_i = 0.1, i = 1, 2,..., 10.

Size class i	1	2	3	4	5
ν_i	0.225	11.57	212.1	803.6	1414
Size class i	6	7	8	9	10
ν_i	2507	3535	5142	8357	19286

Table 2. Eigenvalues (left column) for Black Earth with 10 size classes, divided as equal intervals of log *v*. Parameter values are $\alpha = 100$, $\beta = 50$. The three sections in the table are the 'fast', 'intermediate' and 'slow' eigenvalues (i.e., time scales), with the lists of Estimates and Bounds in the heading referring to these sections, respectively. S_L and S_U are given by Eqs. (A6) and (A7), respectively, and r_i and R_i by Eq. (A2). Note how close the 'fast' values are to the estimates (middle column) of $(v_i + \alpha)$ and the 'slow' values are to either of the bounds (right column) r_i or r_{i-1}.

Eigenvalues (Numerical)	Estimates	Bounds
	$-(v_i + \alpha)$	R_i
	S_U	S_U S_L
	$-\alpha/(v_{i-1} + \alpha)$	r_i
		–19387
–19382	–19386	
		–8458
–8453	–8457	
		–5244
–5239	–5243	
		–3637
–3632	–3636	
		–2608
–2603	–2607	
		–1515
–1510	–1514	
		–904
–899.8	–904	
		–313
–308.9	–312	
		–112
–110.9	–111.6	
		–100.23
–100.21	–100.22	
		–43.86
–38.88	–38.64	
		–38.64
		–0.9977
–0.9975	–0.9978	
		–0.8955
–0.8838	–0.896	
		–0.3197
–0.2940	–0.320	
		–0.1106
–0.1003	–0.111	
		–0.0660
–0.05847	–0.0660	
		–0.03834
–0.03434	–0.0384	
		–0.02750
–0.02364	–0.0275	
		–0.01907
–0.01513	–0.0191	
		–0.01182
–0.007519	–0.0118	
		–0.005158

Supplementary Material: Analysis of the roots of $\beta\bar{K}(s) = -1$

Express $\bar{K}(s)$ from Eq. (16) as:

$$\bar{K}(s) = \sum \frac{\nu_i p_i}{Q(s;\nu_i)}, \qquad Q(s;\nu) = (s+1)(s+\alpha) + s\nu. \tag{A1}$$

The behavior of $K(\tau) = L^{-1}[\bar{K}(s)]$, where L^{-1} is the inverse Laplace transform operator, is determined largely by the roots of the I quadratics, $Q(s;\nu_i)$. The singularities of $\bar{K}(s)$ are given by the roots, r_i and R_i, of $Q(s;\nu_i)$:

$$\begin{bmatrix} r_i \\ R_i \end{bmatrix} = -\frac{\nu_i + \alpha + 1}{2}\left[1 \begin{matrix} - \\ + \end{matrix} \sqrt{1 - \frac{4\alpha}{(\nu_i + \alpha + 1)^2}}\right], \tag{A2}$$

which shows that r_i and R_i are always real and negative since $\alpha,\ \nu_i > 0$.

Our main results are collected in Theorem 1, which builds upon the following Lemmas.

Lemma 1. Let $\alpha > 0$ and $\nu > 0$, then $Q(s;\ \nu)$ has two distinct real negative roots $R(\nu) \in (-\infty, \min(-1, -\alpha))$ and $r(\nu) \in (\max(-1, -\alpha), 0)$. Moreover, $r(\nu)$ is a strictly increasing function, and $R(\nu)$ a strictly decreasing function of ν.

Proof. Note that the notation used in Eq. (A2) is $R_i \equiv R(\nu_i)$ and similarly for r_i. For $\alpha,\ \nu > 0$, the roots r_i and R_i in Eq. (A2) are distinct. Furthermore, since $0 < 4\alpha/(\nu + \alpha + 1)^2 < 1$, r_i and R_i are real and $R_i < r_i$. Observe that $Q(s;\ \nu) \to \infty$ as $s \to \pm\infty$.

Let ν_i, ν_j be two values of $\nu > 0$, with $\nu_j > \nu_i$, with roots given by R_i, R_j, r_i, r_j. Since:

$$Q(R_i;\nu_j) = (R_i+1)(R_i+\alpha) + R_i\nu_i + R_i(\nu_j - \nu_i) = R_1(\nu_j - \nu_i) < 0, \tag{A3}$$

$Q(s;\ \nu_j)$ has a root $R_j < R_i$. An identical argument shows there is a root $r_j > r_i$. Thus, $R(\nu)$ and $r(\nu)$ are, respectively, decreasing and increasing functions of ν.

Since $Q(-\alpha;\ \nu) = -\alpha\nu < 0$, and $Q(-1;\ \nu) = -\nu < 0$ there is a root $R(\nu) < \min(-1, -\alpha)$ and a root $\max(-1, -\alpha) < r(\nu)$. Similarly, $Q(0,\ \nu) = \alpha > 0$, so there is a root $r(\nu) < 0$.

Remark 1.1. Observe that as $\nu \to \infty, R(\nu) \to -\infty$ and $r(\nu) \uparrow 0$.

Remark 1.2. It is also straightforward to show that $Q(s;\ \nu) < 0$ for $R(\nu) < s < r(\nu)$.

Remark 1.3. Tighter bounds on R_i and r_i can be obtained from Eq. (A2). For example, $-1 - \nu_i - \alpha < R_i < -\nu_i + \min(-1, -\alpha)$ and $\max(-1, -\alpha/(1 + \nu_i)) < r_i < -\alpha/(1 + \nu_i + \alpha)$.

Lemma 2. The function $\bar{K}(s)$ is smooth except at $s = R_i \equiv R(\nu_i)$ and $s = r_i \equiv r(\nu_i)$. At these singularities,

$$\lim_{s \to R_i^{\pm}} \bar{K}(s) = \mp\infty; \quad \lim_{s \to r_i^{\pm}} \bar{K}(s) = \mp\infty. \tag{A4}$$

Proof. By inspection.

Remark 2.1. Lemma 1 shows that the singularities are all distinct. For convenience, we index the roots R and r differently. Starting from the most negative R root, the numbering is ordered, $I, I - 1, \ldots, 1$. Starting from the most negative r root, the numbering is $1, 2, \ldots, I$. With this indexing, we have, from Lemma 1:

$$R_I < \ldots < R_2 < R_1 < \min(-1, -\alpha) < \max(-1, -\alpha) < r_1 < r_2 < \ldots < r_I < 0. \tag{A5}$$

Then, R_I and r_I correspond to the largest ν, R_{I-1} and r_{I-1} to the second largest value of ν, etc. Combining this with Remark 1.2, we see that each term in $\bar{K}(s)$ is negative for $s \in (R_1, r_1)$ and so $\bar{K}(s) < 0$ in this range. Since $\bar{K}(s)$ is continuous and bounded above on this interval, it attains a maximum value somewhere. Let this maximum value be $-1/\beta^*$, with $\beta^* > 0$, attained for some value $s = s^* \in (R_1, r_1)$. This s^* is unique, as shown below.

We now localize the roots:

Lemma 3. There is at least one root of $\beta\bar{K}(s) = -1$ in each of the $I - 1$ intervals (R_{i+1}, R_i), and in each of $I - 1$ intervals (r_i, r_{i+1}).

Proof. Use Lemma 2 and apply the intermediate value theorem on each of the stated intervals. The function $\bar{K}(s)$ takes on every real value on each of the intervals; in particular, it takes on the value $-1/\beta$ at some point(s) in each interval.

Remark 3.1. $\beta\bar{K}(s) = -1$ has $2I$ roots. Lemma 3 shows that at least $I - 1$ 'fast' roots (i.e., higher magnitude, denoted by R_i) are found in $s \in (-\infty, \min(-1, -\alpha))$ and at least $I - 1$ 'slow' roots (i.e., lower magnitude, denoted by r_i) are in $s \in (\max(-1, -\alpha), 0)$. We isolate the other two roots below.

Lemma 4. The value $s^* \in (R_1, r_1)$ where $\bar{K}(s)$ attains its maximum value $(-1/\beta^*)$ is unique. If $\beta < \beta^*$ then there is a root of $\beta\bar{K}(s) = -1$ in each of the intervals (R_1, s^*) and (s^*, r_1).

Proof. The value s^* is a stationary point of $\bar{K}(s)$. If $\beta = \beta^*$ then s^* is a real root of $\beta^*\bar{K}(s)$ = -1 with multiplicity of at least two. Along with the (at least) $2I - 2$ roots of Lemma 3, this makes at least $2I$ roots. Hence, if there was another s^* there would be more than $2I$ roots, which is impossible.

Remark 4.1. Applying the intermediate value theorem on (R_1, s^*), we see that $\bar{K}(s)$ attains every value in $\left(-\infty, -1/\beta^*\right)$ somewhere on this interval. In particular, it attains the value $-1/\beta$ if $\beta < \beta^*$. The same argument works on (s^*, r_1). Thus, if $\beta < \beta^*$, we have found $2I$ disjoint intervals each containing at least one root. But, there are exactly $2I$ roots of the characteristic equation. Hence, for $\beta < \beta^*$ there is exactly one root in each of the stated intervals.

Remark 4.2. At $\beta = \beta^*$, the roots coalesce into a double real root, while for $\beta > \beta^*$, there are two complex roots. To complete the analysis of the location of the roots of $\beta\overline{K}(s) = -1$, we need to specify the magnitude of β^* relative to α and β. For this, observe that $s = -\alpha$ is in the interval (R_1, r_1) (Lemma 1), and that $\overline{K}(-\alpha) = -1/\alpha$. But, since $-1/\beta^*$ is the maximum value of $\overline{K}$ on (R_1, r_1), this means that $-1/\beta^* \geq -1/\alpha$, or $\beta^* \geq \alpha$. We also have the physical condition that the eroded soil is always more easily eroded than the original soil, i.e., $\beta < \alpha$. Thus, $\beta < \alpha \leq \beta^*$ or, in words, the value of β never exceeds β^*, meaning that double (or complex) roots cannot occur.

Remark 4.3. From Lemmas 3 and 4, we conclude that there is exactly one root in each of $I - 1$ intervals (R_{i+1}, R_i), and in each of $I - 1$ intervals (r_i, r_{i+1}). There are two distinct roots in the interval (R_1, r_1).

We now show how all the roots vary as a function of detachability β.

Lemma 5. The leftmost (rightmost) I roots strictly increase (decrease) with β for $\beta \in (0, \beta^*)$.

Proof. Since $\overline{K}(s)$ has one root for $s \in (R_i, R_{i+1})$, from Lemma 2 $\overline{K}(s)$ is strictly increasing on this interval. Since $-1/\beta$ increases with increasing β, so must the root of $\overline{K}(s) = -1/\beta$. A corresponding argument applies to the case $s \in (r_i, r_{i+1})$.

We now consider the pair of roots in $s \in (R_1, r_1)$.

Lemma 6. Given that $\alpha > \beta > 0$, the two roots of $\overline{K}(s) = -1/\beta$ are located in (R_1, r_1) as follows:

I $\alpha > \beta > 1$; one in $(R_1, -\alpha)$ and one in $(-\alpha, -1)$.

II $\alpha > 1 > \beta > 0$; one in $(R_1, -\alpha)$ and one in $(-1, r_1)$.

III $1 > \alpha > \beta > 0$; one in $(R_1, -1)$ and one in $(-\alpha, r_1)$.

Proof. For I: From Lemma 2, $\lim_{s \downarrow R_1} \bar{K}(s) = -\infty$ and, from Lemma 1, $R_1 < -\alpha$. Since $\bar{K}(-\alpha) = -1/\alpha > -1/\beta$, the intermediate value theorem shows there exists $s \in (R_1, -\alpha)$ satisfying $\bar{K}(s) = -1/\beta$. Also, $\bar{K}(-1) = -1 < -1/\beta$ by hypothesis, and again the intermediate value theorem shows existence of a root in $(-\alpha, -1)$.

For II: From Lemma 2, $\lim_{s \uparrow r_1} \bar{K}(s) = -\infty$ and, from Lemma 1, $r_1 > -1$. Since $\bar{K}(-1) = -1 > -1/\beta$ for this case, the intermediate value theorem shows existence of a root in $(-1, r_1)$. Since $-\alpha < -\beta$ and $\bar{K}(-\alpha) = -1/\alpha > -1/\beta$, the intermediate value theorem shows there is a root in $(R_1, -\alpha)$.

For III: From Lemma 2, $\lim_{s \downarrow R_1} \bar{K}(s) = -\infty$ and, from Lemma 1, $R_1 < -1$. Since $\bar{K}(-1) = -1 > -1/\beta$ for this case, the intermediate value theorem shows there is a root in $(R_1, -1)$. Also, from Lemma 1, $r_1 > -\alpha$. Recalling that $\bar{K}(-\alpha) = -1/\alpha > -1/\beta$ and $\lim_{s \uparrow r_1} \bar{K}(s) = -\infty$, the intermediate value theorem shows there is root in $(-\alpha, r_1)$.

Remark 6.1. If $\beta = 1$ then $s = -1$ is a root of $\beta\bar{K}(s) = -1$. Similarly, if $\alpha = \beta$ (meaning that the deposited soil has the same cohesion as the original soil, which is not physically realistic), then $s = -\alpha$ is a root.

By this sequence of Lemmas, the following theorem is proved.

Theorem 1. Assume $p_i > 0$, $\alpha > \beta > 0$. The $2I$ roots of $\bar{K}(s) = -1/\beta$ have the properties:

(i) All the roots are real, simple and negative.

(ii) There are I roots in the interval $(-\infty, \min(-\alpha, -1))$.

(iii) There are $I - 1$ roots in the interval $(\max(-\alpha, -1), 0)$.

(iv) The location of the final root depends on the values of α and β relative to –1 as specified in Lemma 6.

Roots in (ii) are denoted as fast, those in (iii) are called slow. We refer to the root in (iv) as the intermediate root. The bounds on this root for $\alpha > \beta > 1$ can be far apart, particularly if $\alpha \gg 1$. The bounds for this case are sharpened below.

Theorem 2. Let $\alpha > \beta > 0$, then lower, s_L, and upper, s_U, bounds on the intermediate root are given by

$$s_L > \max\left(s_{\min}, s_{\max} - \frac{\beta \sum \frac{v_i p_i}{r_i - R_i}}{1 - \beta \sum \frac{v_i p_i}{(s_{\min} - R_i)(r_i - R_i)}} \right), \tag{A6}$$

and

$$s_U < \min\left(s_{\max}, r_I - \frac{\beta \sum \frac{v_i p_i}{r_i - R_i}}{1 - \beta \sum \frac{v_i p_i}{(s_{\max} - R_i)(r_i - R_i)}} \right), \tag{A7}$$

where, from Lemma 6, $(s_{\min}, s_{\max})$ are defined as:

$$(s_{\min}, s_{\max}) = \begin{cases} (-\alpha, -1), & \alpha > \beta > 1 \\ (-1, r_1), & \alpha > 1 > \beta \\ (-\alpha, r_1), & 1 > \alpha > \beta. \end{cases} \tag{A8}$$

Proof. Write $\beta \bar{K}(s) = -1$ as

$$-\frac{1}{\beta}=\sum_{i=1}^{I}\frac{v_i p_i}{r_i-R_i}\left(\frac{1}{s-r_i}-\frac{1}{s-R_i}\right). \tag{A9}$$

For the lower bound Eq. (A9) becomes

$$\begin{aligned}-\frac{1}{\beta}&>\sum_{i=1}^{I}\frac{v_i p_i}{r_i-R_i}\left(\frac{1}{s-r_i}-\frac{1}{s_{\min}-R_i}\right)\\&>\sum_{i=1}^{I}\frac{v_i p_i}{r_i-R_i}\left(\frac{1}{s-s_{\max}}-\frac{1}{s_{\min}-R_i}\right),\end{aligned} \tag{A10}$$

which on rearranging for *s* gives the bound of inequality (A6). The upper bound is found analogously as

$$\begin{aligned}-\frac{1}{\beta}&<\sum_{i=1}^{I}\frac{v_i p_i}{r_i-R_i}\left(\frac{1}{s-r_i}-\frac{1}{s_{\max}-R_i}\right)\\&<\sum_{i=1}^{I}\frac{v_i p_i}{r_i-R_i}\left(\frac{1}{s-r_I}-\frac{1}{s_{\max}-R_i}\right),\end{aligned} \tag{A11}$$

resulting in inequality (A7)

Theorem 3. $\bar{K}(s)$ has an upper bound of *B*/*s*.

Proof. Since

$$(s+1)(s+\alpha)+sv>s(\alpha+v+1), \tag{A12}$$

then,

$$\bar{K}(s)=\sum\frac{v_i p_i}{(s+1)(s+\alpha)+sv_i}<\frac{1}{s}\sum\frac{v_i p_i}{\alpha+v_i}=\frac{B}{s}. \tag{A13}$$

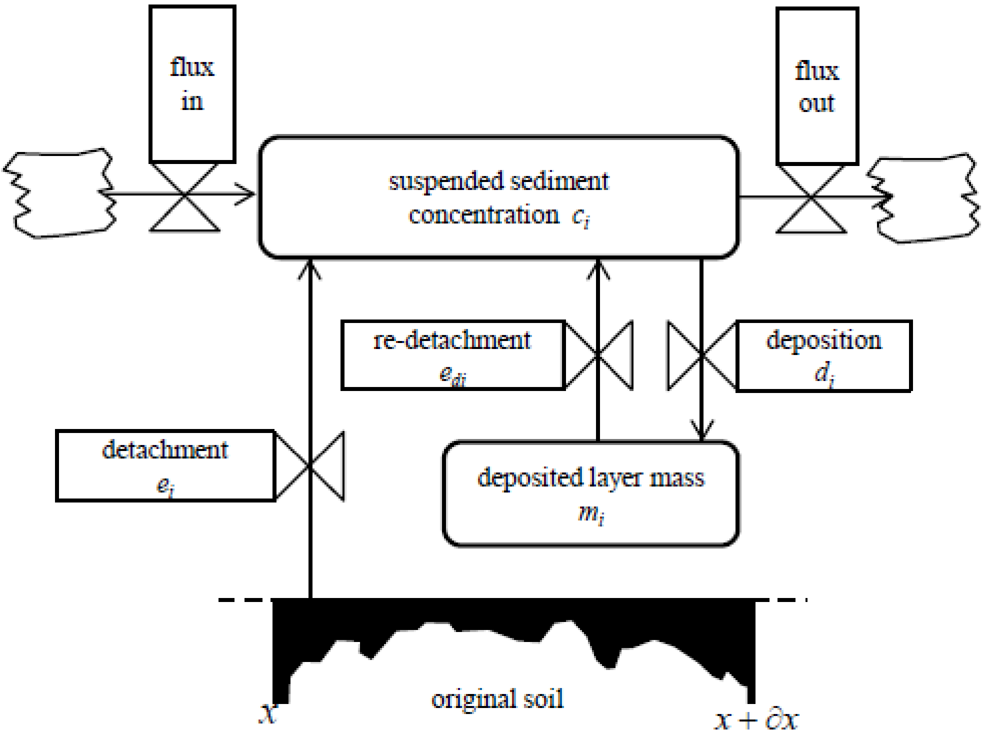

flux in
flux out
suspended sediment concentration c_i
re-detachment e_{di}
deposition d_i
detachment e_i
deposited layer mass m_i
original soil
x
$x + \partial x$

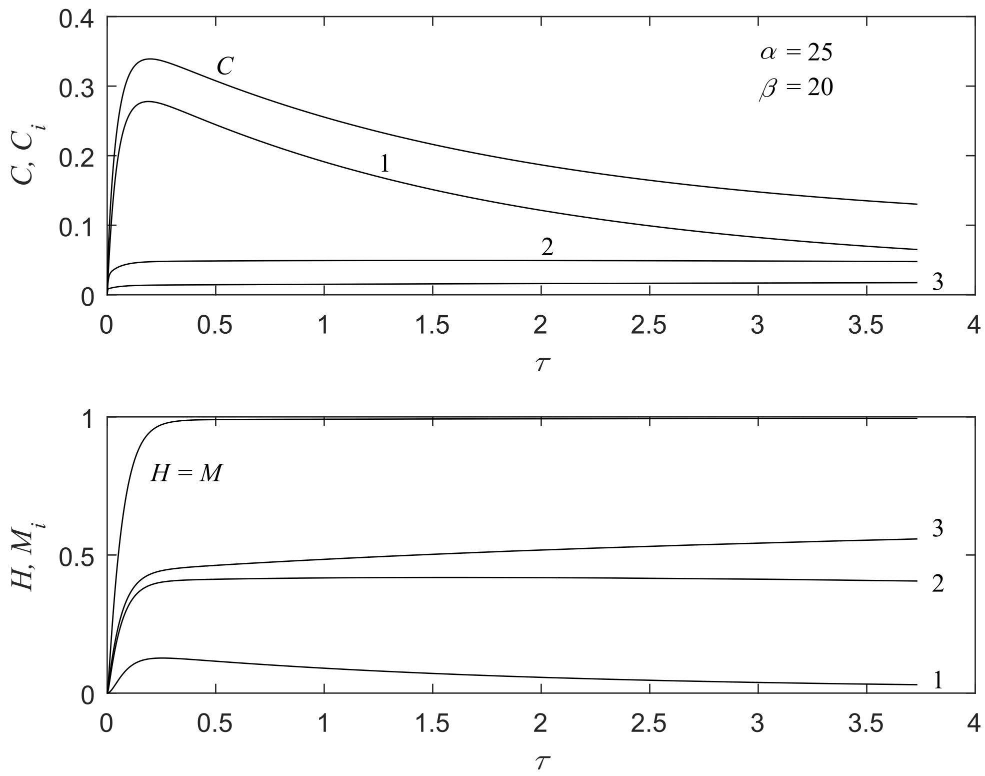

$\alpha = 25$
$\beta = 20$
C
1
2
3
C, C_i
0.4
0.3
0.2
0.1
0
0.5
1
1.5
2
2.5
3
3.5
4
τ
$H = M$
3
2
1
H, M_i
1
0.5
0
τ

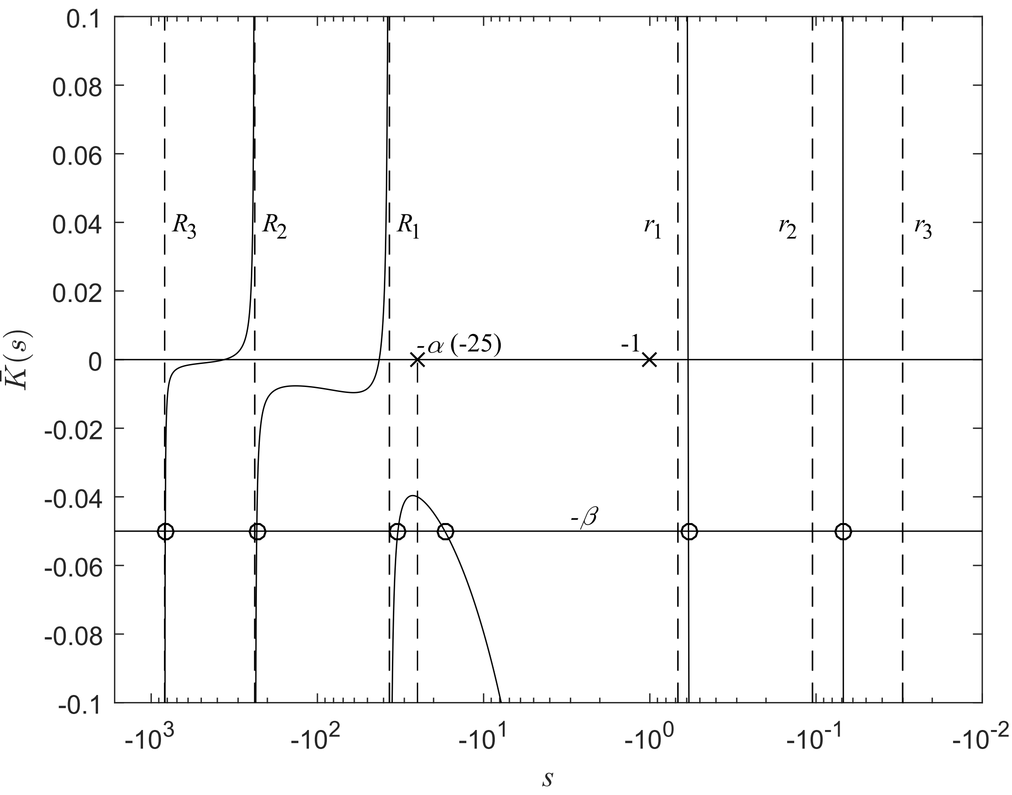
0.1
0.08
0.06
0.04
0.02
0
-0.02
-0.04
-0.06
-0.08
-0.1
$\bar{K}(s)$
R_3
R_2
R_1
r_1
r_2
r_3
-α (-25)
-1
-β
-10^3
-10^2
-10^1
-10^0
-10^{-1}
-10^{-2}
s

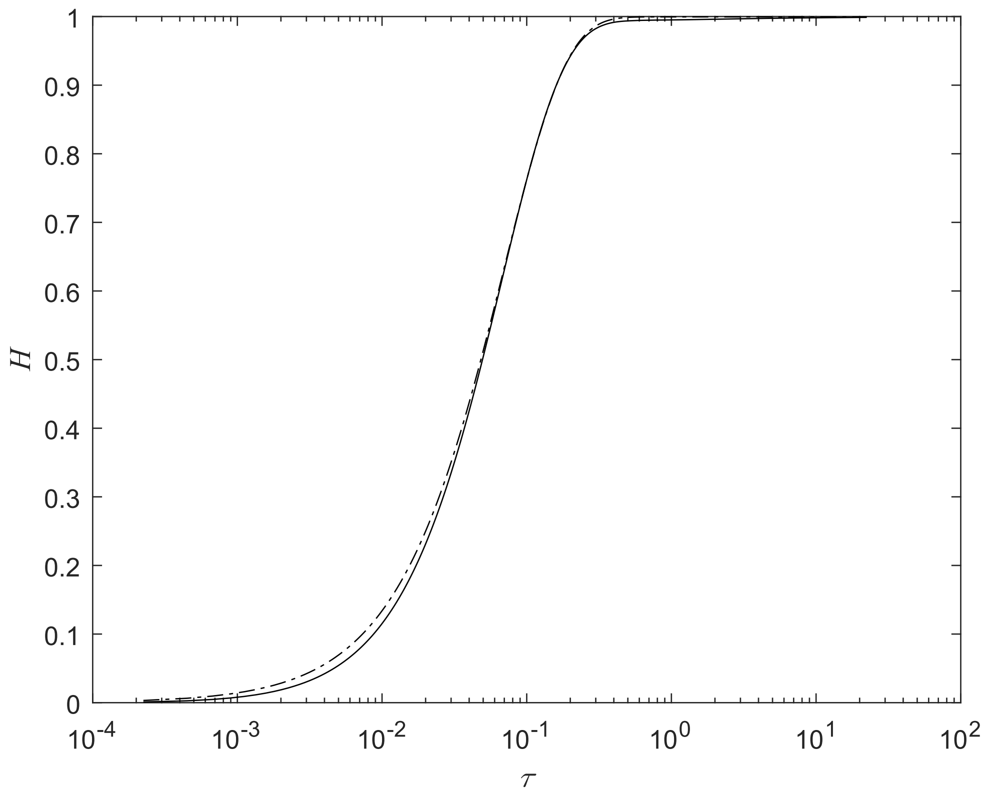

1
0.9
0.8
0.7
0.6
0.5
0.4
0.3
0.2
0.1
0
H
10^{-4}
10^{-3}
10^{-2}
10^{-1}
10^{0}
10^{1}
10^{2}
τ

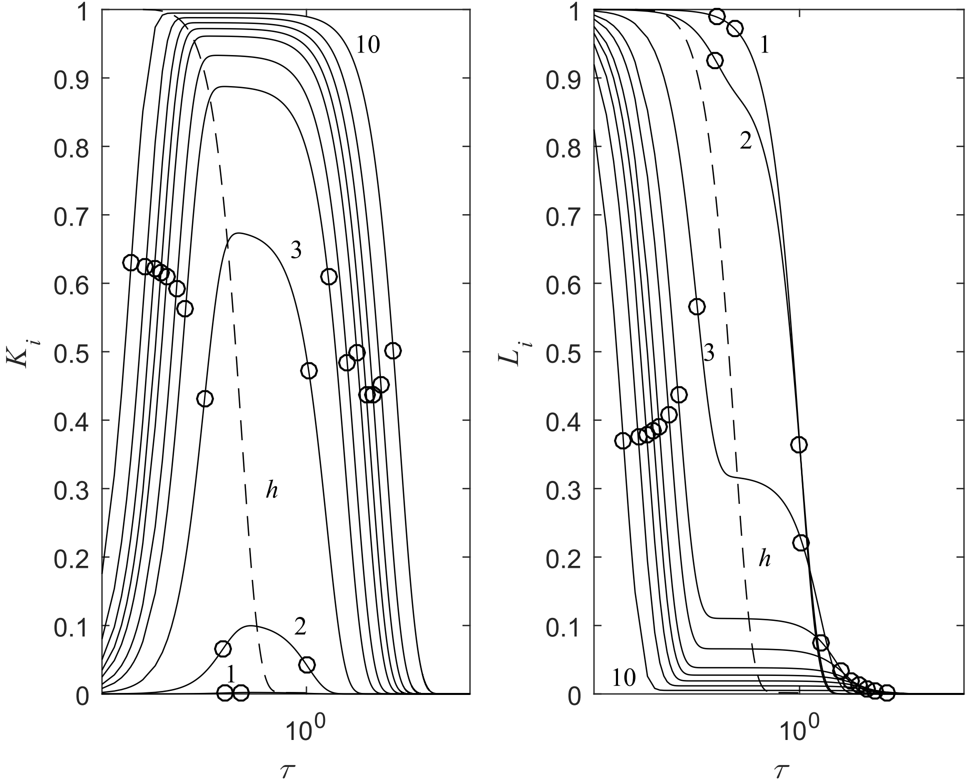

1
0.9
0.8
0.7
0.6
0.5
0.4
0.3
0.2
0.1
0
K_i
10
3
h
2
1
10^0
τ
L_i
1
2
3
h
10
10^0
τ